
Chapter 4: Observations: Changes in Snow, Ice and Frozen Ground

Coordinating Lead Authors: Peter Lemke (Germany), Jiawen Ren (China)

Lead Authors: Richard Alley (USA), Ian Allison (Australia), Jorge Carrasco (Chile), Gregory Flato (Canada), Yoshiyuki Fujii (Japan), Georg Kaser (Austria), Philip Mote (USA), Robert Thomas (USA), Tingjun Zhang (USA)

Contributing Authors: Jason Box (USA), David Bromwich (USA), Ross Brown (Canada), Graham Cogley (Canada), Joey Comiso (USA), Mark Dyurgerov (USA), Blair Fitzharris (New Zealand), Oliver Frauenfeld (USA), Helen Fricker (USA), Hilmar Gudmundsson (UK), Christian Haas (Germany), Jan-Ove Hagen (Norway), Charles Harris (UK), Larry Hinzman (USA), Regine Hock (Sweden), Martin Hoelzle (Switzerland), Philippe Huybrechts (Belgium), Ketil Isaksen (Norway), Peter Jansson (Sweden), Adrian Jenkins (UK), Ian Joughin (USA), Christoph Kottmeier (Germany), Ron Kwok (USA), Seymour Laxon (UK), Shiyin Liu (China), Douglas MacAyeal (USA), Humphrey Melling (Canada), Atsumu Ohmura (Switzerland), Anthony Payne (UK), Terry Prowse (Canada), Bruce Raup (USA), Charlie Raymond (USA), Eric Rignot (USA), Ignatius Rigor (USA), David Robinson (USA), Drew Rothrock (USA), Simon Scherrer (Switzerland), Sharon Smith (Canada), Olga Solomina (Russia), David Vaughan (UK), John Walsh (USA), Anthony Worby (Australia), Tomomi Yamada (Japan), Lin Zhao (China)

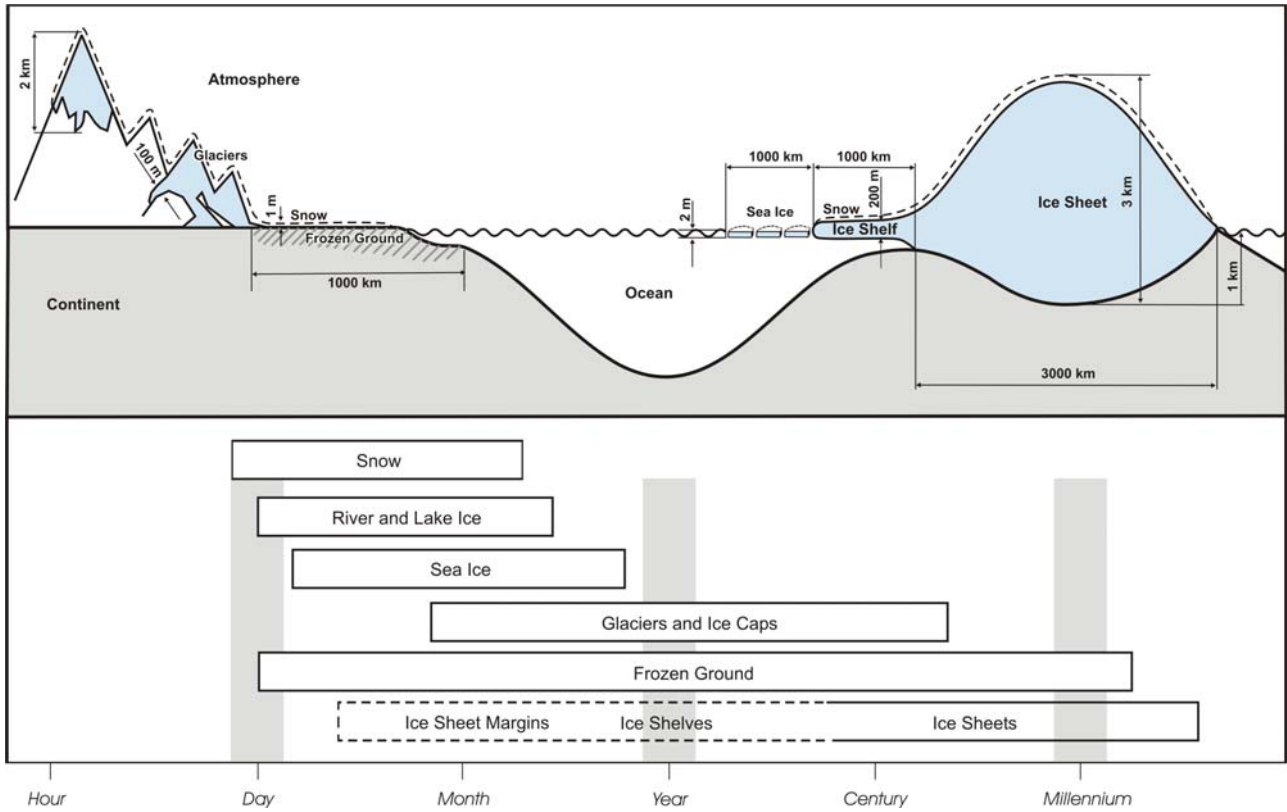
Review Editors: Roger Barry (USA), Toshio Koike (Japan)

Date of Draft: 2 March 2006

Notes: TSU compiled version

1 **Figures**

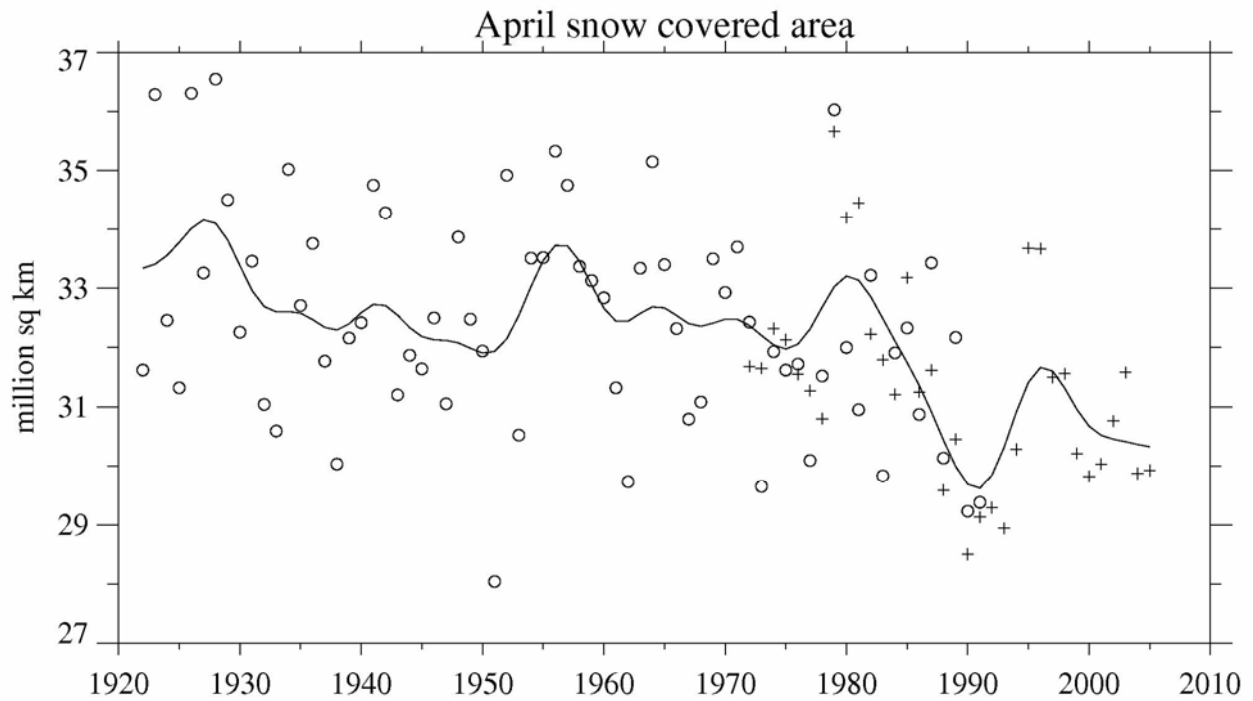
2
3



4
5
6
7

Figure 4.1.1. Components of the cryosphere and their time-scales.

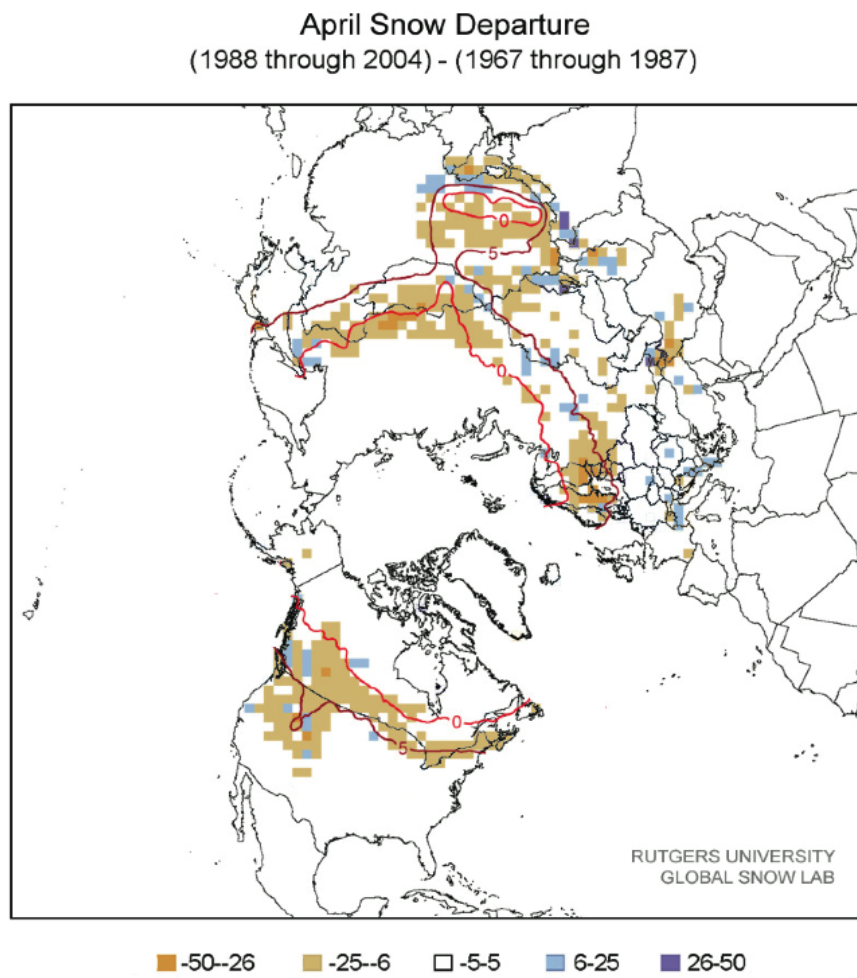
1
2



3
4
5
6
7
8

Figure 4.2.1. Update of NH April snow covered area (SCA) from Brown (2000). Open circles are from the station-derived snow cover index of Brown (2000); plus symbols are SCA values from the NOAA satellite dataset. The smooth curve is derived using the same 13-point filter as in Chapter 3.

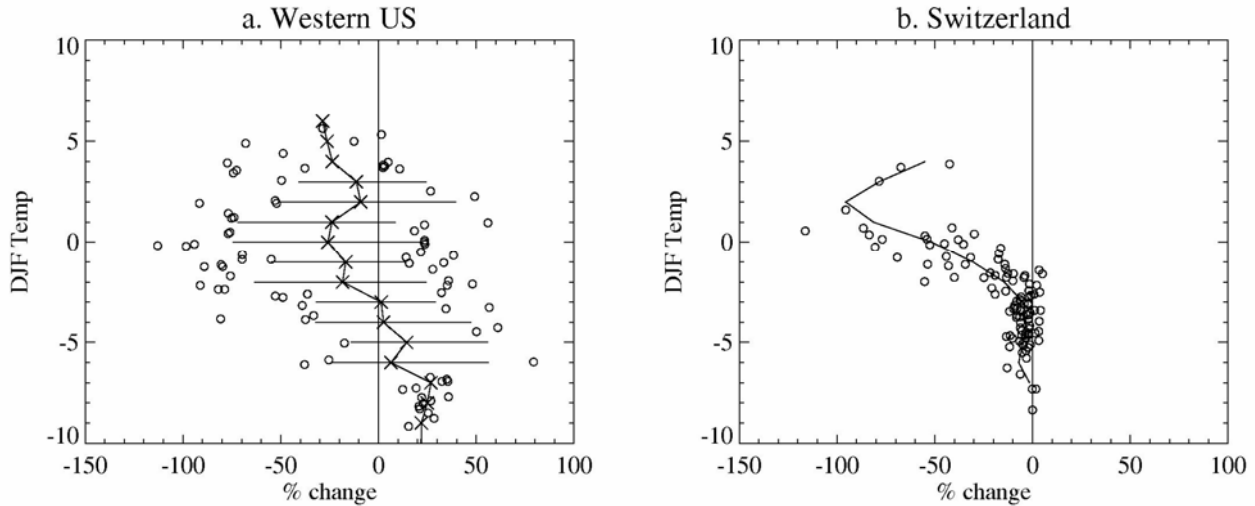
1
2



3
4
5
6
7
8

Figure 4.2.2. Differences in the distribution of April snow cover between earlier (1967–1987) and later (1988–2004) portions of the satellite era (expressed in percent coverage). Negative values indicate greater extent in the earlier portion of the record. Extents are derived from NOAA/NESDIS snow maps.

1

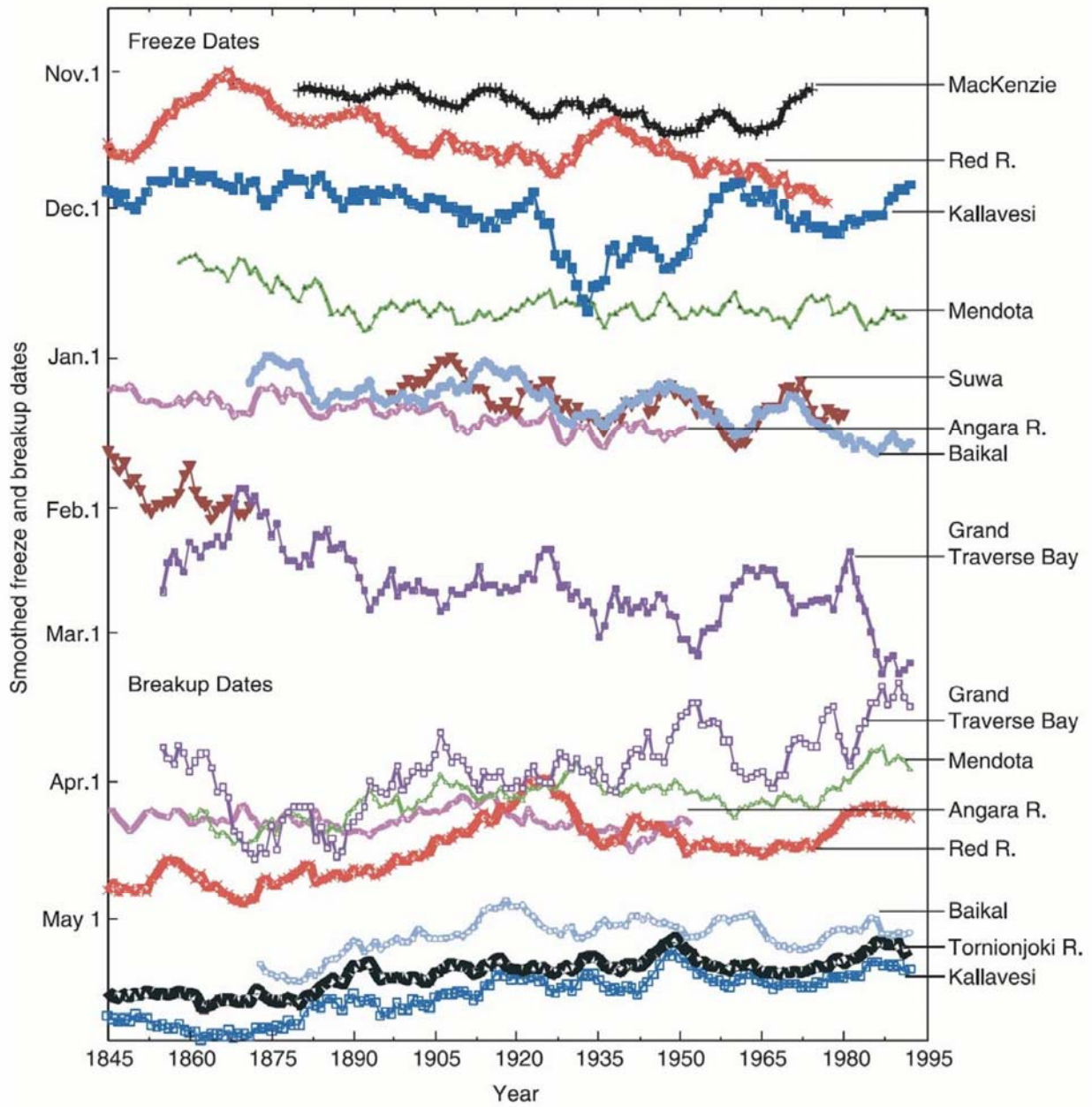


2
3

4 **Figure 4.2.3.** Dependence of trends in snow on mean winter temperature (°C) at each location. (a) Relative
5 trends in 1 April snow water equivalent, 1950–2000, in the mountains of western North America (British
6 Columbia, Washington, Oregon, and California), binned by mean December–February (DJF) temperature.
7 For each 1°C temperature bin, ‘x’ symbols indicate the mean trend, bars indicate the span from the 10th
8 percentile to the 90th percentile for bins with at least 10 points, and circles indicate outliers. Total number of
9 data points is 323. Adapted from Mote et al. (2005). (b) Relative trend in days of winter (December-
10 February) snow cover at 109 sites in Switzerland, 1958–1999, binned by mean DJF temperature. Adapted
11 from Scherrer et al., 2004.

12

1
2



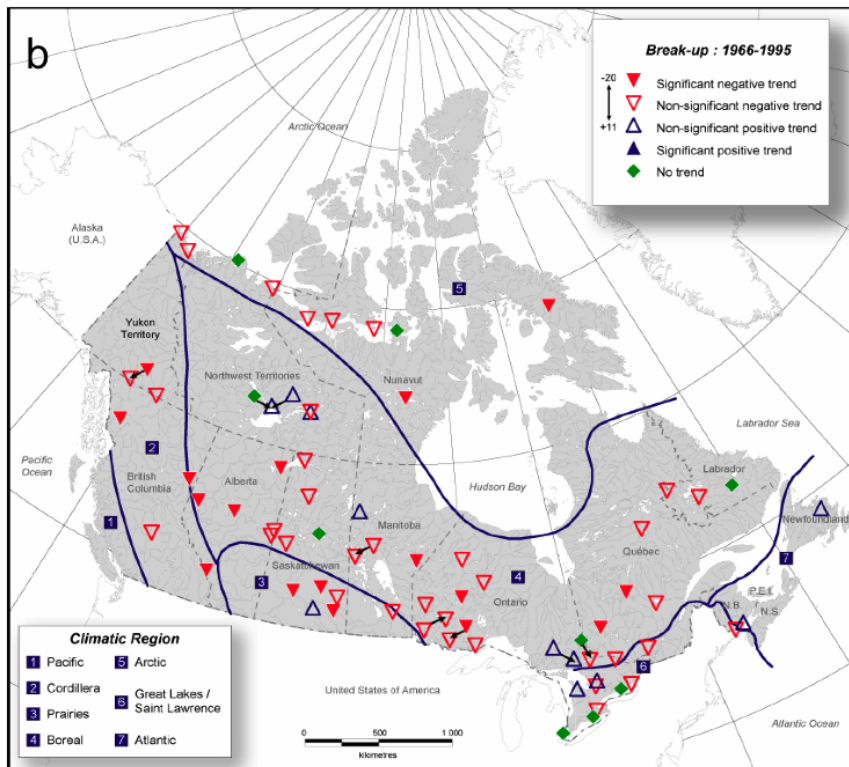
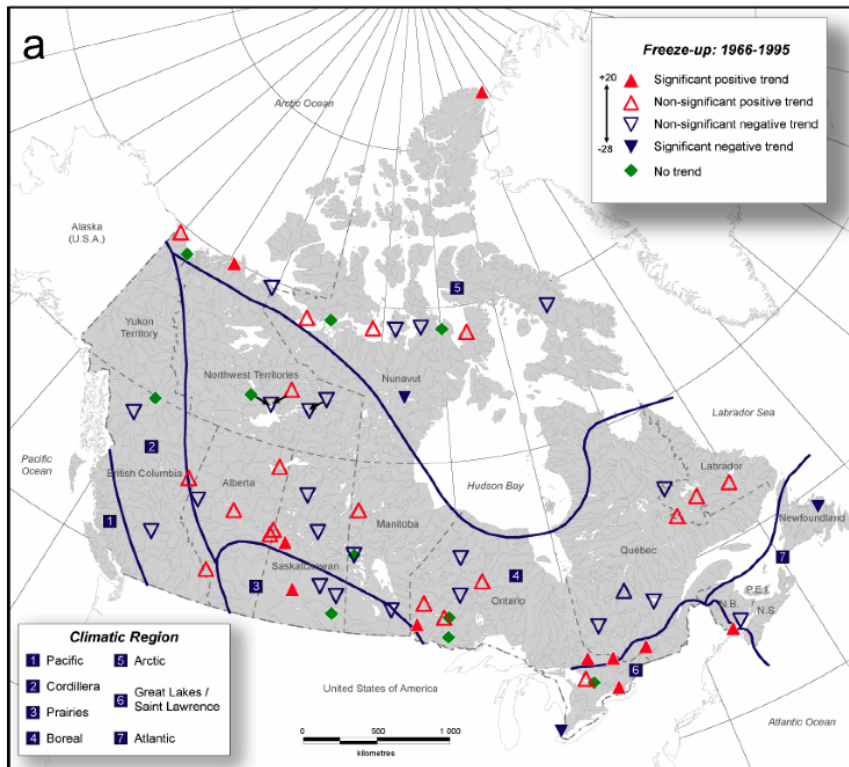
3
4
5
6
7
8

Figure 4.3.1. Time series of freeze-up and break-up dates from several northern lakes and rivers (from Magnuson et al., 2000). Dates have been smoothed with a 10-year moving average. See the cited publication for locations and other details.

1
23
4
5
6
7
8
9

Figure 4.3.2. Trends in river ice-cover duration. Upward pointing triangle indicate lengthening of the ice-cover period while downward triangle indicate shortening of the ice-cover period. Trends significant at the 1% and 10% levels are marked by larger filled and hollow triangles, respectively. Smaller triangles indicate trends that are not significant at the 10% level (Zhang et al., 2001).

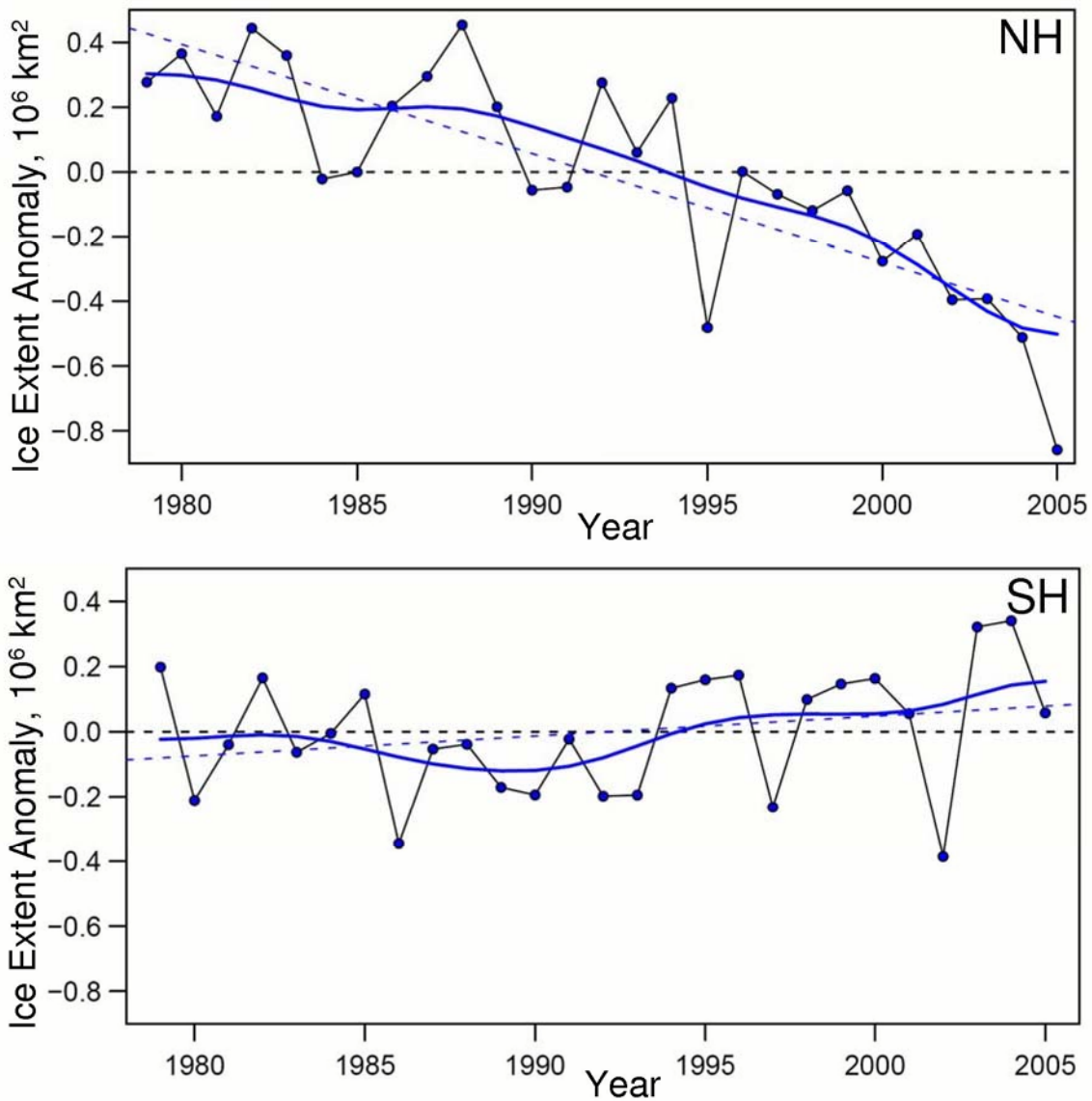
1
2



3
4
5
6
7
8
9
10

Figure 4.3.3. Trends in freeze-up and break-up dates observed at lakes in Canada over the period 1965–1995. Downward pointing arrows indicate a negative trend; upward pointing arrows a positive trend. Open symbols indicate that the trend is not significant while solid symbols indicate that the trend is significant at the 10% level. The shading indicates the trend in date when the zero-degree temperature threshold is crossed. From Duguay et al. (2006).

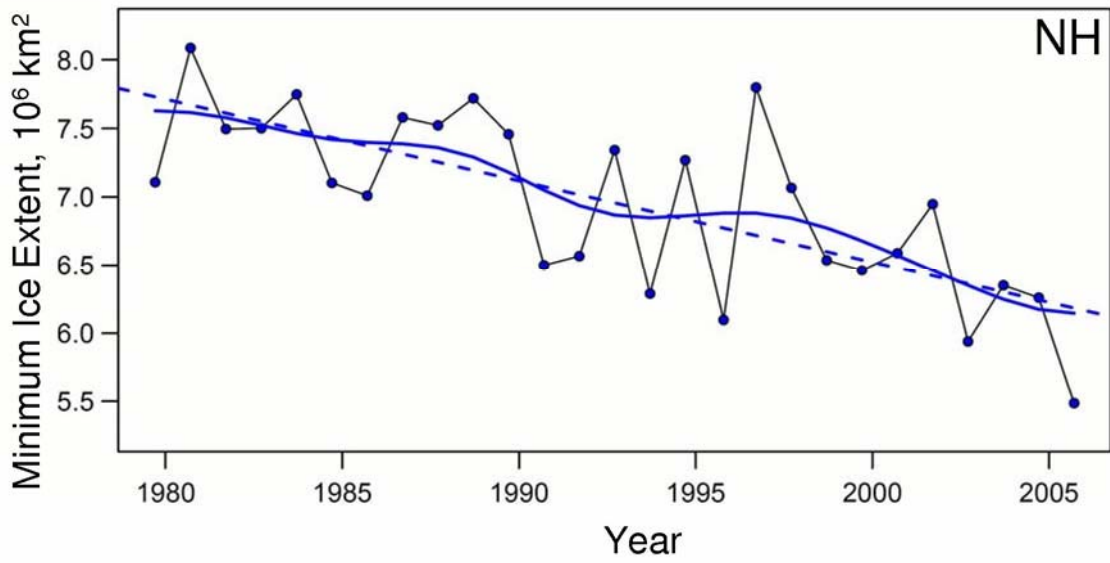
1
2



3
4
5
6
7
8
9
10
11
12

Figure 4.4.1. Sea Ice extent anomalies for (a) Northern Hemisphere and (b) the Southern Hemisphere based on passive microwave satellite data. Symbols indicate annual mean values while the curve is the result of a 13-point time filter. Linear trend lines are indicated for each hemisphere. For the Arctic, the trend is $-33 \pm 8.8 \times 10^3 \text{ km}^2$ per year (equivalent to approximately -2.6% per decade), whereas the Antarctic results show a small positive trend of $5.6 \pm 11 \times 10^3 \text{ km}^2$ per year. The negative trend in the Northern Hemisphere is significant at the 95% confidence level whereas the small positive trend in the Southern Hemisphere is not significant. (Updated from Comiso, 2003).

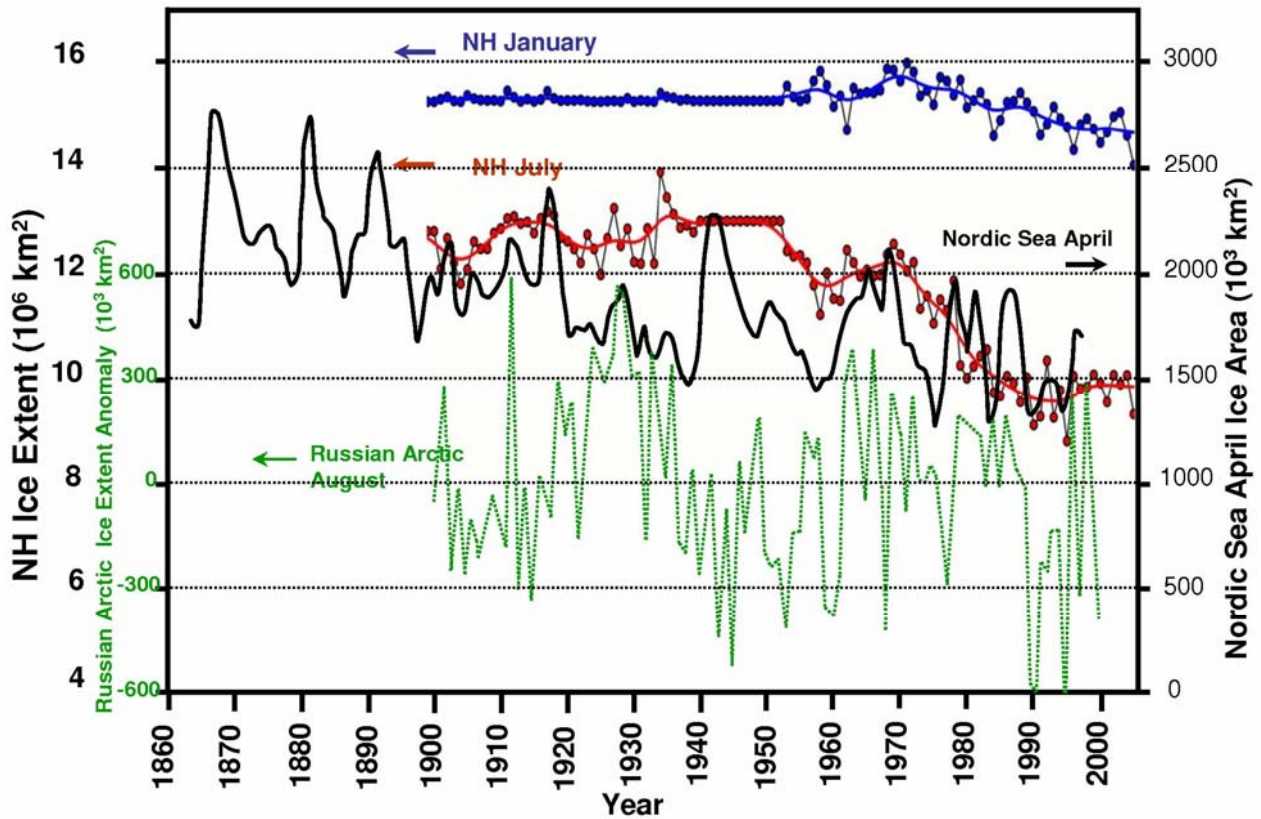
1
2



3
4
5
6
7
8

Figure 4.4.2. Summer minimum Arctic ice extent from 1979 to 2005. Symbols indicate annual mean values while the curve is the result of a 13-point time filter. The dashed line indicates the linear trend which is $-60 \pm 24 \times 10^3 \text{ km}^2$ per year, or approximately -8% per decade (updated from Comiso, 2002).

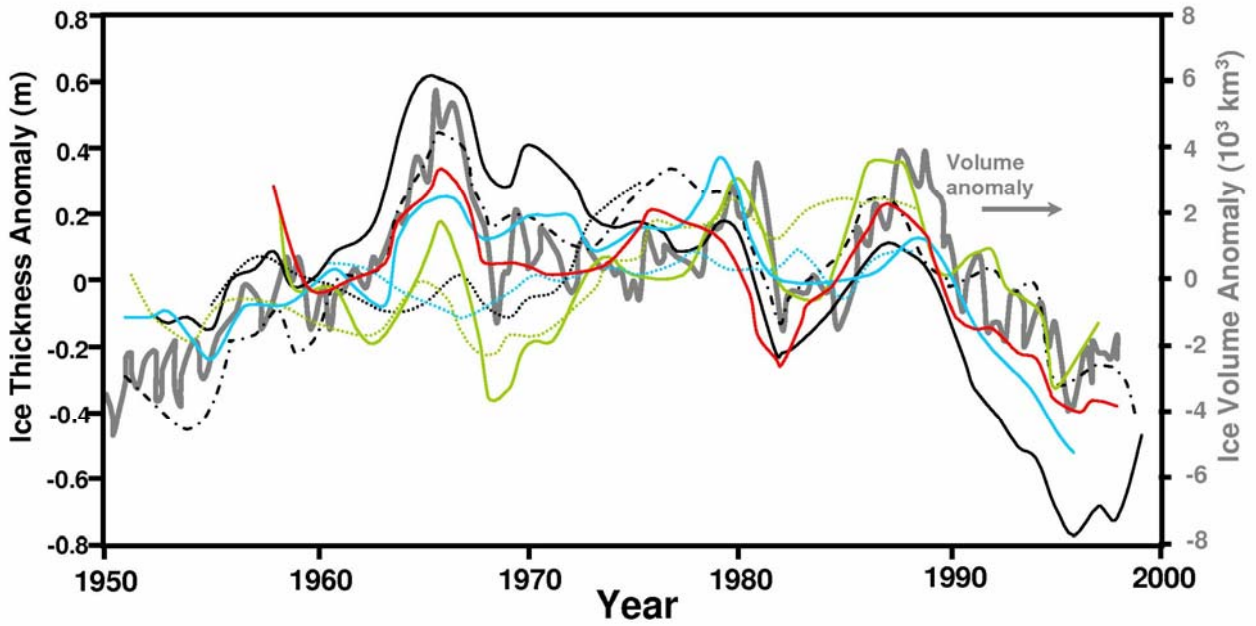
1
2



3
4
5
6
7
8
9
10
11

Figure 4.4.3. Time series of Northern Hemisphere ice extent for January and July from the HadISST data set (the blue and red curves, updated from Rayner et al., 2003), the April Nordic Sea ice extent (the black curve, redrafted from Vinje, 2001), and the August ice extent anomaly in the Russian Arctic seas -- Kara, Laptev, East Siberian and Chukchi -- the dotted green curve, redrafted from Polyakov et al., (2003). For the Northern Hemisphere time series, the symbols indicate yearly anomalies while the curve is the result of a 13-point time filter.

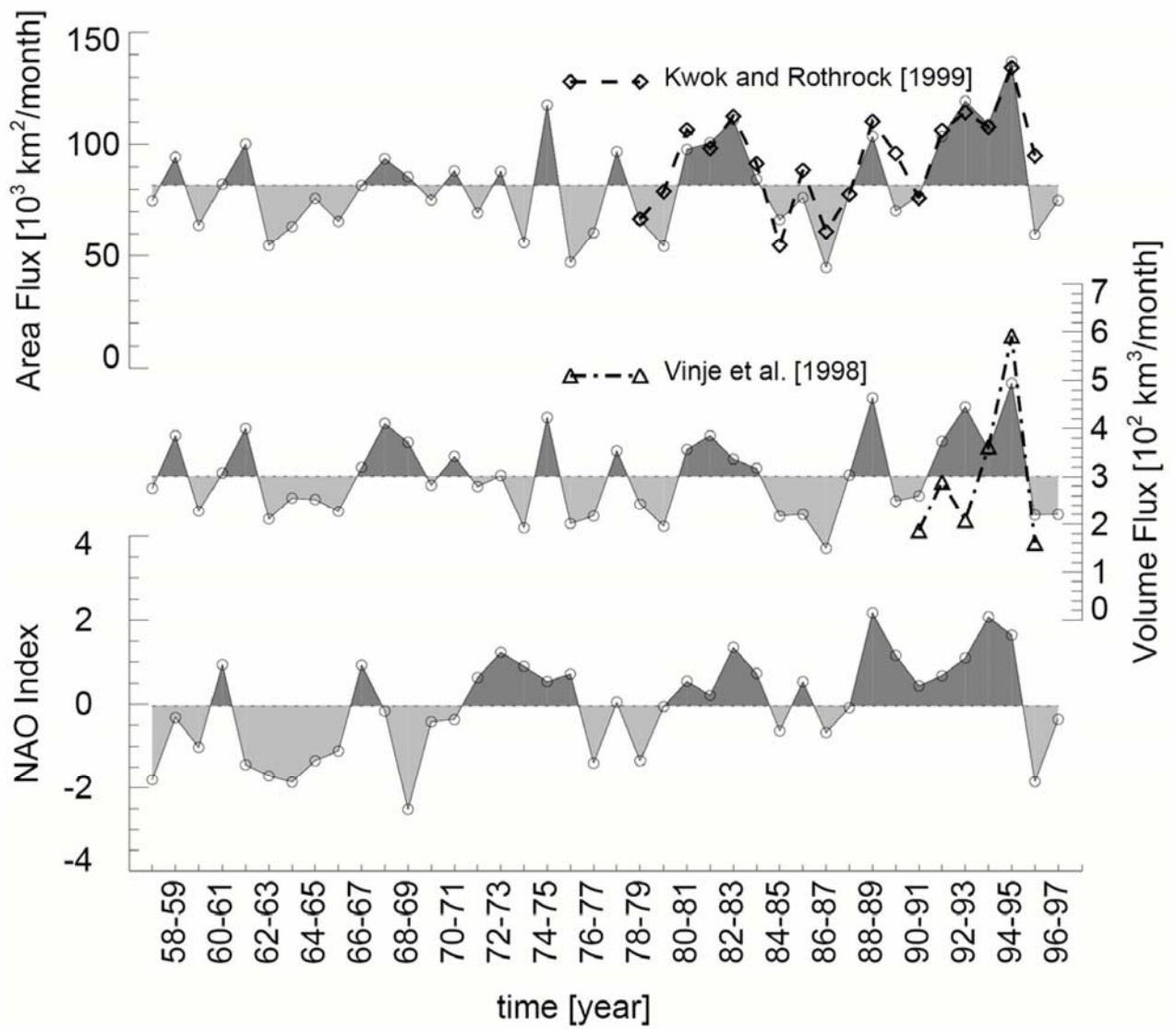
1
2



3
4
5
6
7
8
9
10

Figure 4.4.4. Comparison of model-based time series of annual mean, Arctic-basin average ice thickness anomaly), obtained from a variety of models (redrafted from Rothrock et al., 2003 – see this paper for identification of the individual models and their attributes), along with the Arctic basin ice volume anomalies (grey curve and right-hand scale) computed by Koeberle and Gerdes (2003).

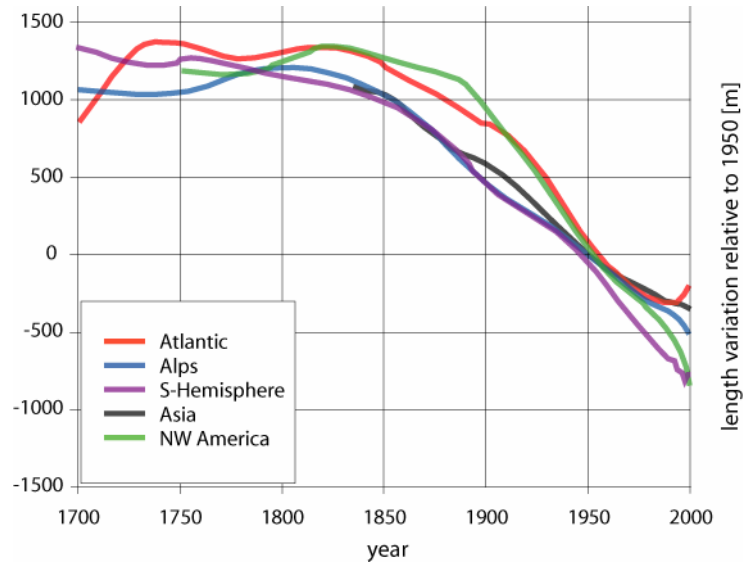
1
2



3
4
5
6
7
8

Figure 4.4.5. Time series of modelled Fram Strait area and volume flux, along with NAO index. Also shown are observational estimates of area flux (Kwok and Rothrock, 1999) and volume flux (Vinje et al., 1998). This figure is reproduced from Hilmer and Jung (2000).

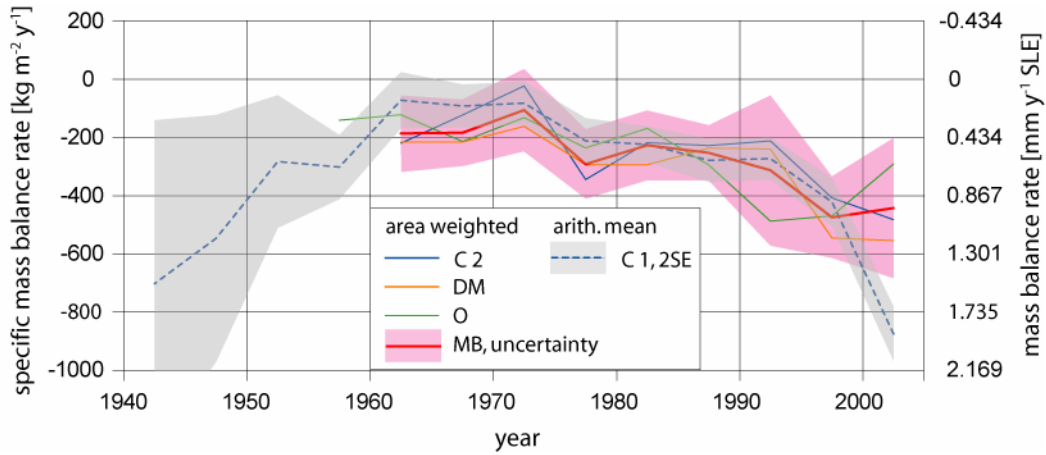
1
2



3
4
5
6
7

Figure 4.5.1. Large scale regional mean length variations of glacier tongues (Oerlemans, 2005). The raw data are all constrained to pass through zero at 1950; the Stineman-smoothed curves (shown) approximate this.

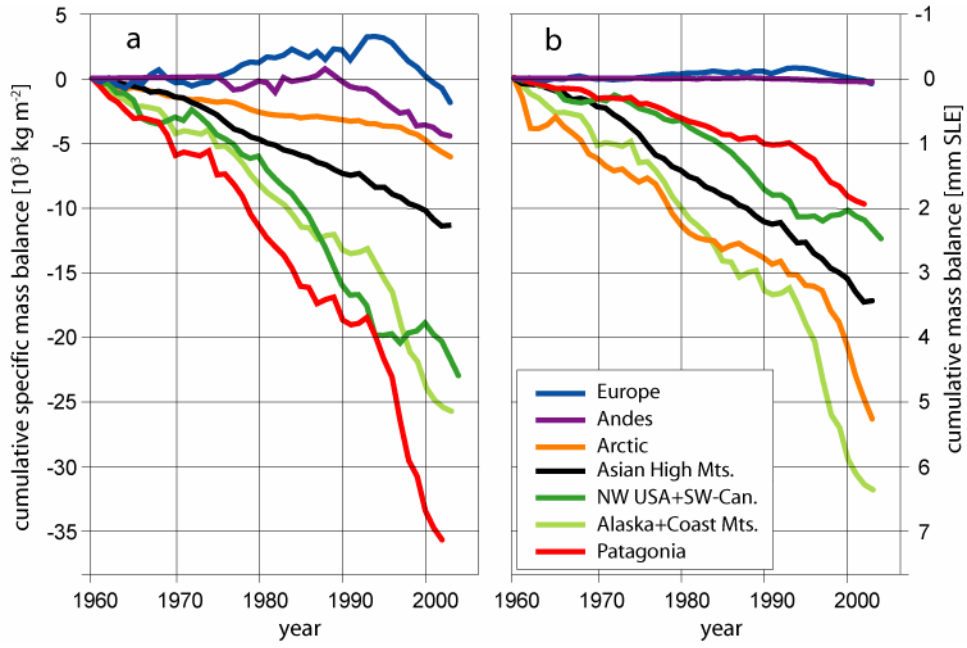
1
2



3
4
5
6
7
8
9
10
11
12
13
14
15
16
17
18
19
20
21
22

Figure 4.5.2. Pentadal average mass balance rates of the world’s glaciers and ice caps excluding those around the ice sheets of Greenland and Antarctica.. The grey shading around the arithmetic mean of the available mass-balance data from numerous glaciers (C1) is twice the standard-error uncertainty, hence twice the standard deviation of the data divided by the square root of the number of glaciers observed. The grey shading thus represents the spatial variability of the measured mass balances of glaciers. Essentially the same data were aggregated in spatial interpolation and area weighted ways in the C2, O, and DM reconstructions. The red shading includes this methodological uncertainty as well as the spatial variability, and is calculated as the square root of the sum of twice the squared spatial standard error and twice the squared standard deviation of the three reconstructions. MB is the respective arithmetic mean. The red shading thus shows the uncertainty in the specific mass balance (the loss/gain of mass per square meter of glacier), hence the uncertainty in the climate signal. The total uncertainty in glacier contribution to sea-level change is obtained by combining this specific-mass-balance uncertainty with the large uncertainty in total glacier area. Data sources: Cogley (2005), Dyurgerov and Meier (2005), Ohmura (2004). The authors made area weighting and spatial interpolation only after 1960, when up to 100 measured mass balances were available. Conversion between specific mass balance rates (mass change rates averaged over the entire glacier area) and mass balance rates uses the ratio of the total surface area of glaciers and ice caps ($785 \cdot 10^3 \text{ km}^2$) and the ocean surface area ($362 \cdot 10^6 \text{ km}^2$).

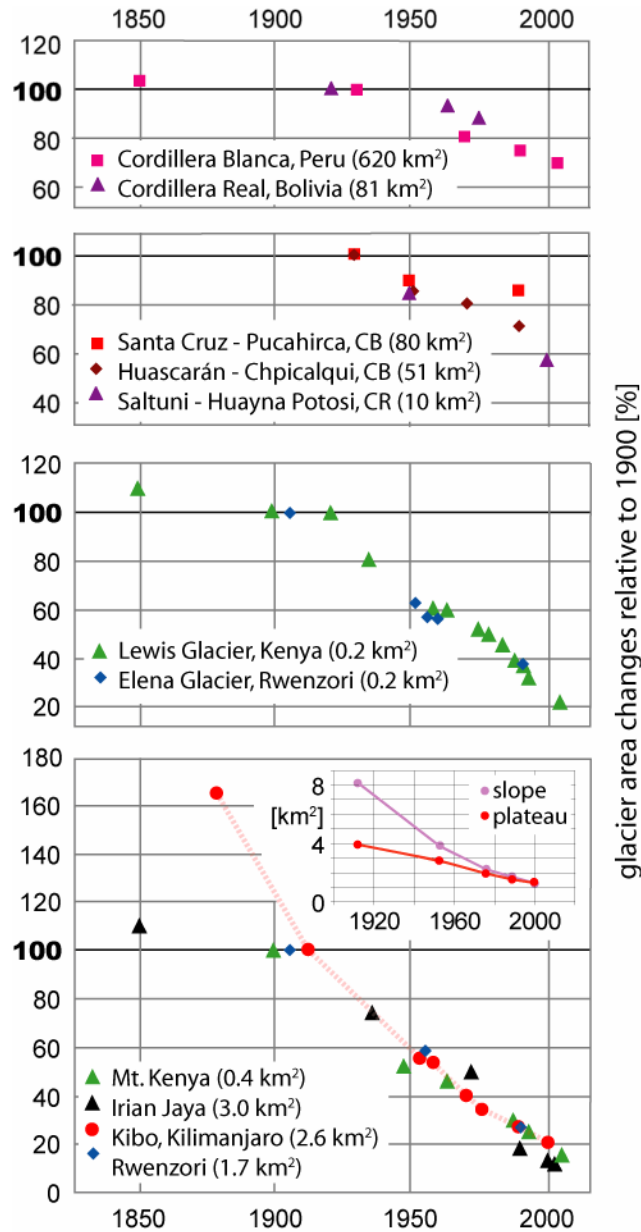
1
2



3
4
5
6
7
8

Figure 4.5.3. Cumulative specific mass balances (a) and cumulative mass balances (b) of glaciers and ice caps, calculated for large regions (Dyurgerov and Meier, 2005). Specific mass balance shows the strength of climate change in the respective region. Cumulative mass balance is the contribution from each region to sea-level rise.

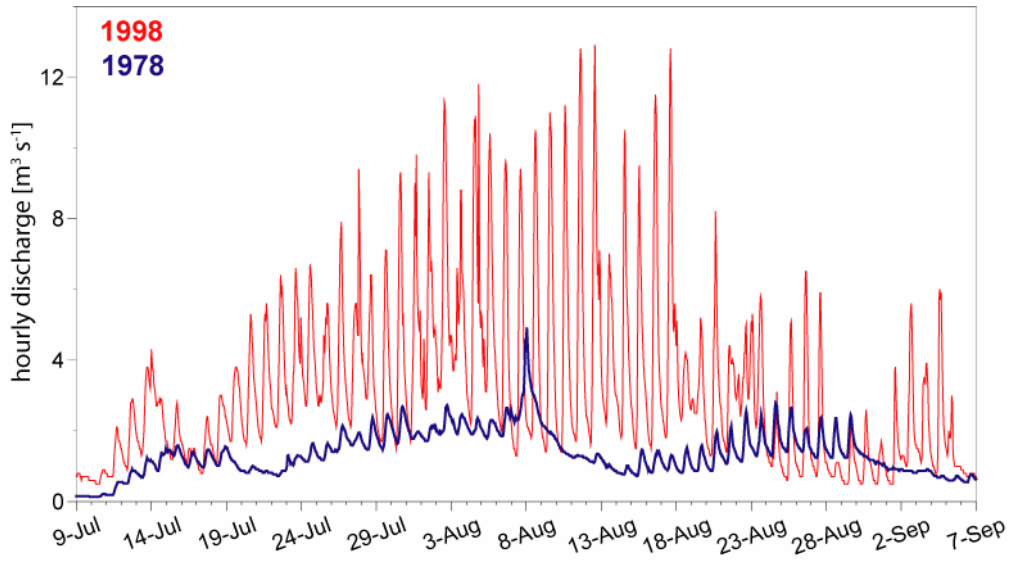
1
2



3
4
5
6
7
8
9
10
11

Figure 4.5.4. Changes in surface area of tropical glaciers relative to their extent around 1900, grouped according to different glacier sizes. The sizes are given for 1990 or the date closest to 1990 available. The broken red line highlights the retreat of Kilimanjaro glaciers. The small insert shows the absolute area change of Kilimanjaro plateau (red) and slope (black) glaciers as separated by the 5700 m contour line. (Georges, 2004; Hastenrath, 2005; Kaser and Osmaston, 2002; Mölg et al., 2003; Thompson et al., 2002) Additional data are from A. Klein and S. Lieb.

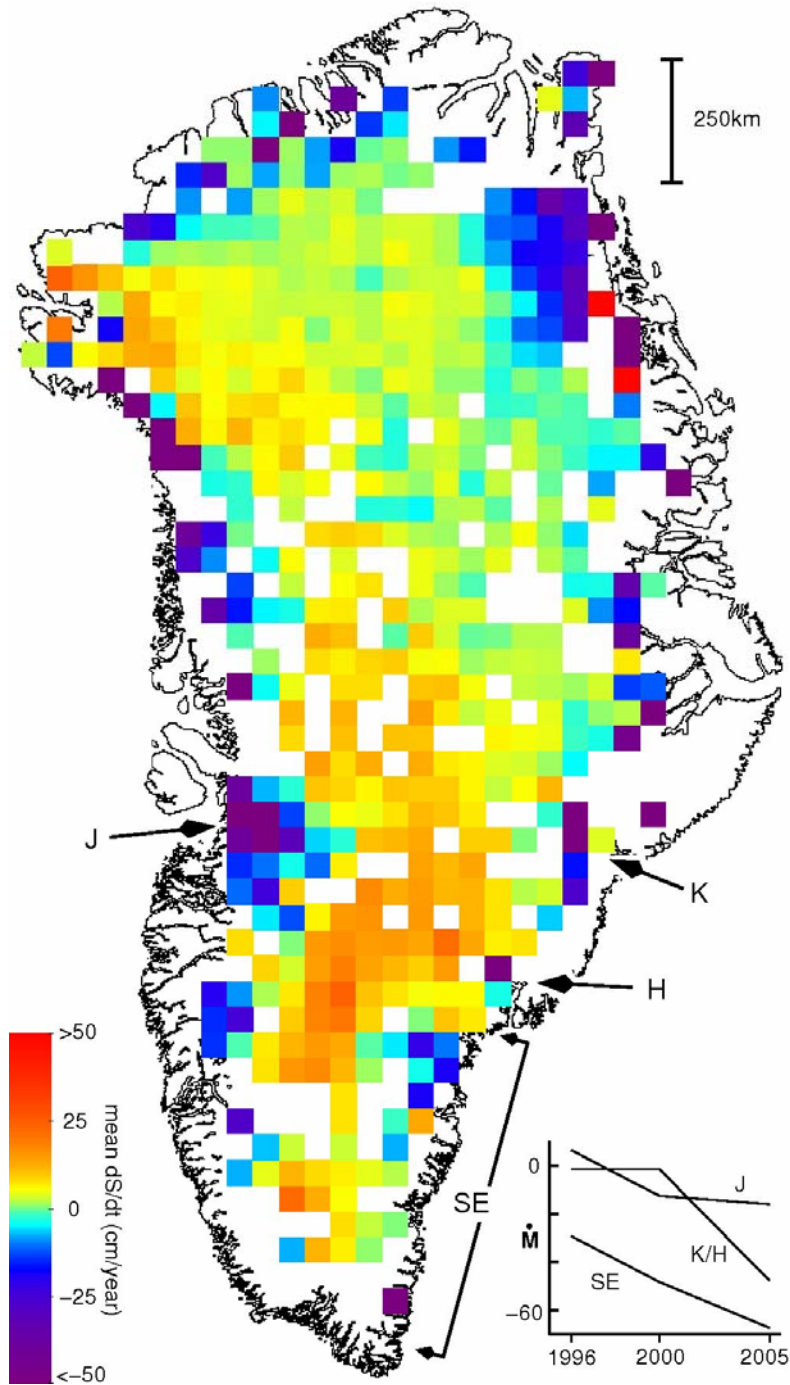
1
2



3
4
5
6
7

Figure 4.5.5. Observed effects of prolonged glacier mass loss on daily discharge of Vernagtferner, Austria. (Data source: Bavarian Academy of Science, Glaciology, <http://www.glaziologie.de/>).

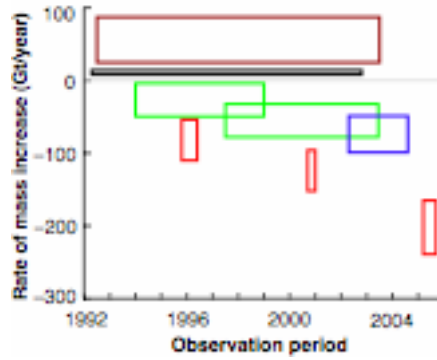
1
2



3
4
5
6
7
8
9
10

Figure 4.6.1. Rates of elevation change (dS/dt) derived from laser-altimeter measurements at more than 16000 locations on the Greenland Ice Sheet where ICESat data from 2005 overlay aircraft surveys in 1998/9 using methods described by Thomas et al. (in press). Locations of rapidly-thinning outlet glaciers at Jakobshavn (J), Kangerdlugssuaq (K), Helheim (H) and along the southeast coast (SE) are shown, together with plots showing their estimated mass balance versus time (Rignot and Kanagaratnam, 2006).

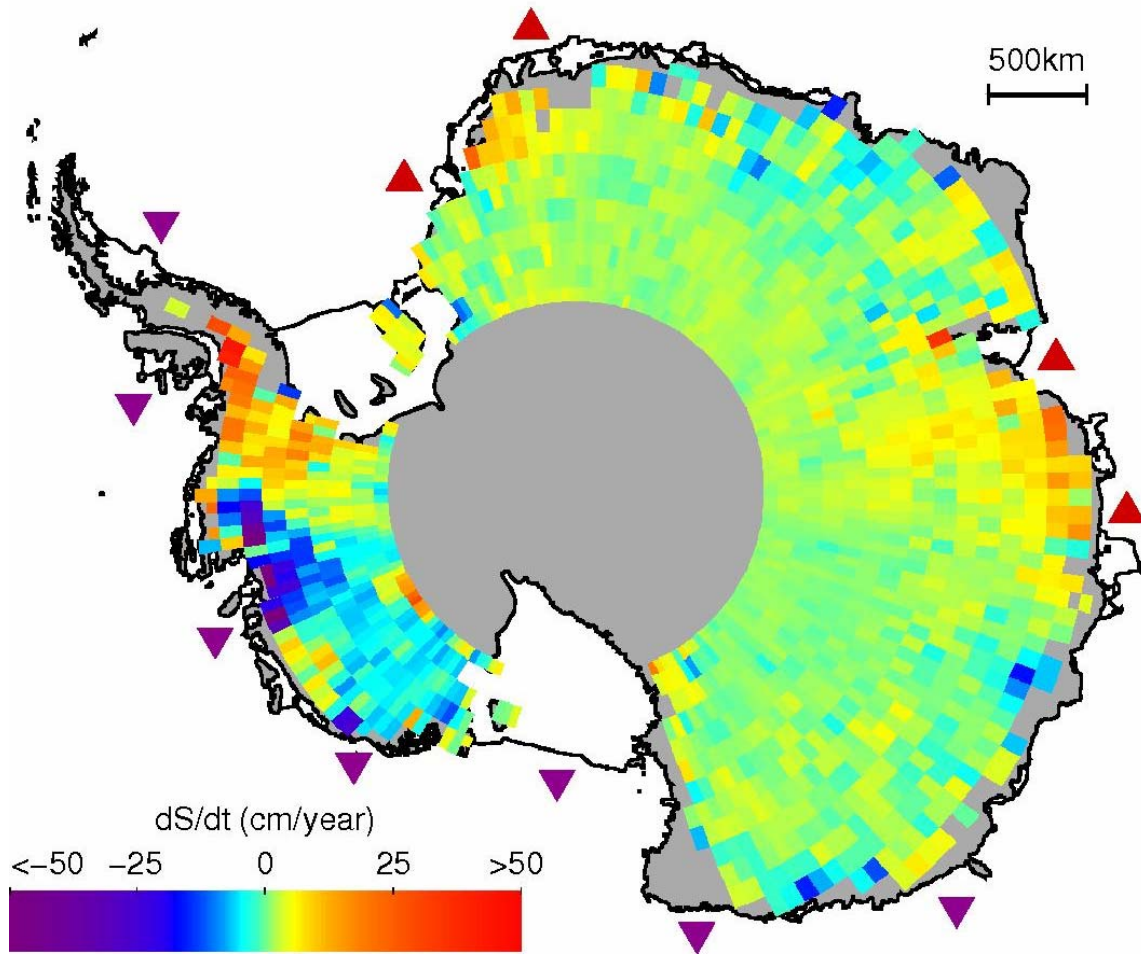
1
2



3
4
5
6
7
8
9
10
11
12

Figure 4.6.2. Estimates of mass balance for the entire Greenland ice sheet. Green - ATM (Krabill et al., 2000; 2004); blue – GRACE (Velicogna and Wahr, 2005); red - mass budget (Rignot and Kanagaratnam, in press); brown - using SRALT-derived values of rates of elevation change in Johannessen et al. (2005); black – from SRALT, combined with ATM (Zwally et al., in press). Uncertainty limits are as published, with those for ATM and Johannessen et al. assuming high-elevation thickening by firn of density $600 \pm 300 \text{ kg m}^{-3}$, low-elevation thinning of ice at density 900 kg m^{-3} , and basal uplift rates of $0 \pm 1 \text{ mm a}^{-1}$.

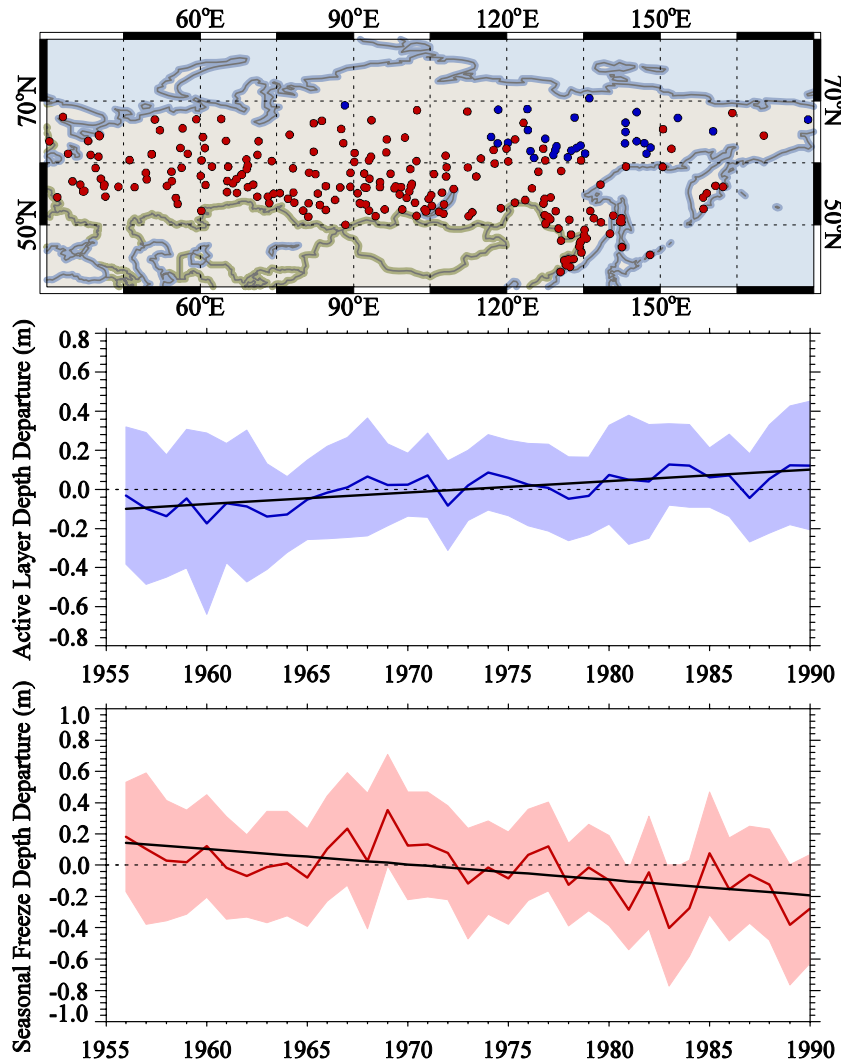
1
2



3
4
5
6
7
8
9
10

Figure 4.6.3. Rates of elevation change (dS/dt) derived from ERS radar-altimeter measurements between 1992 and 2003 over the Antarctic Ice Sheet (Davis et al., 2005). Locations of ice shelves estimated to be thickening or thinning by more than 30 cm a^{-1} (Zwally et al., in press) are shown by purple triangles (thinning) and red triangles (thickening).

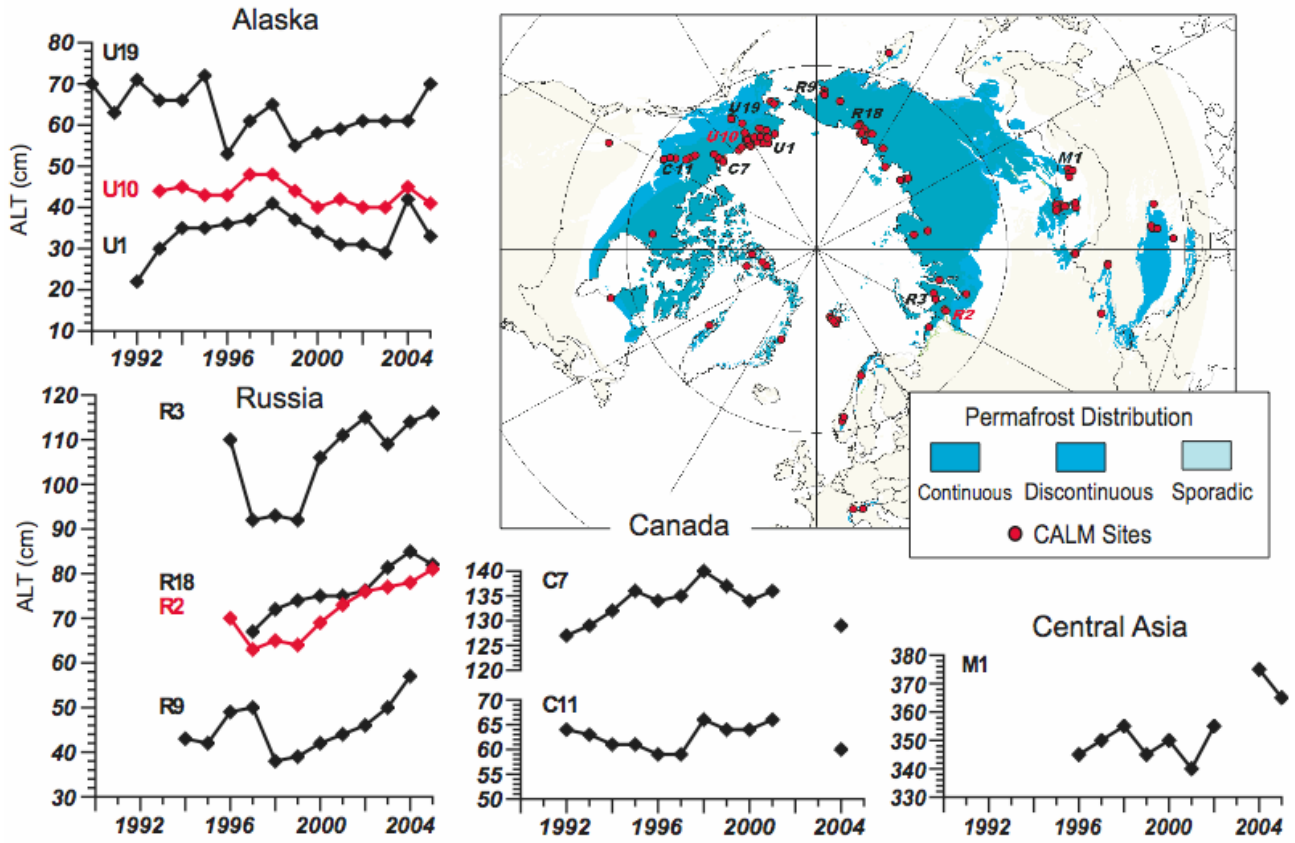
1
2



3
4
5
6
7
8
9
10
11
12
13
14

Figure 4.7.1. Variations of the thickness of the active layer over permafrost (middle) and maximum soil freeze depth in non-permafrost area (lower) in Russia from 1956 through 1990. Active layer thickness has increased about 21 cm while seasonally freeze depth has decreased about 35 cm over the period of record (black lines in middle and lower panels). Anomaly of active layer thickness (thin blue line) is an average of anomalies from 31 stations (blue dots on the top panel) after removing the mean over the period of record for each station. Anomaly of maximum soil freeze depth is an average of anomalies from 211 stations (red dots on the top panel) after removing the mean over the period of record for each station. The shaded area represents the standard deviation from the mean at each year, while dashed-line is the zero reference (From Frauenfeld et al., 2004).

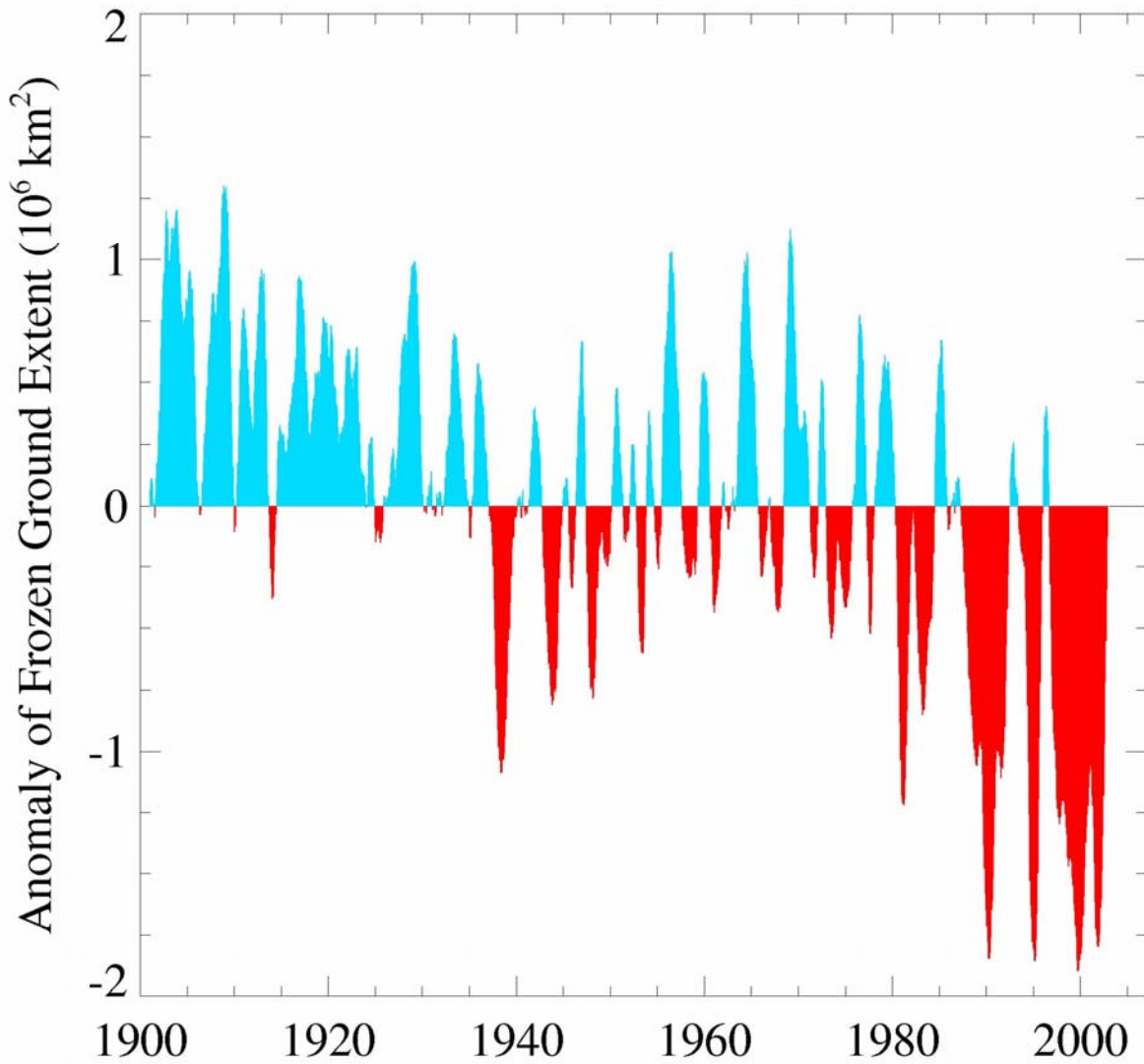
1
2



3
4
5
6
7

Figure 4.7.2. Locations of sites and changes in active layer thickness from selected sites (after Nelson, 2004).

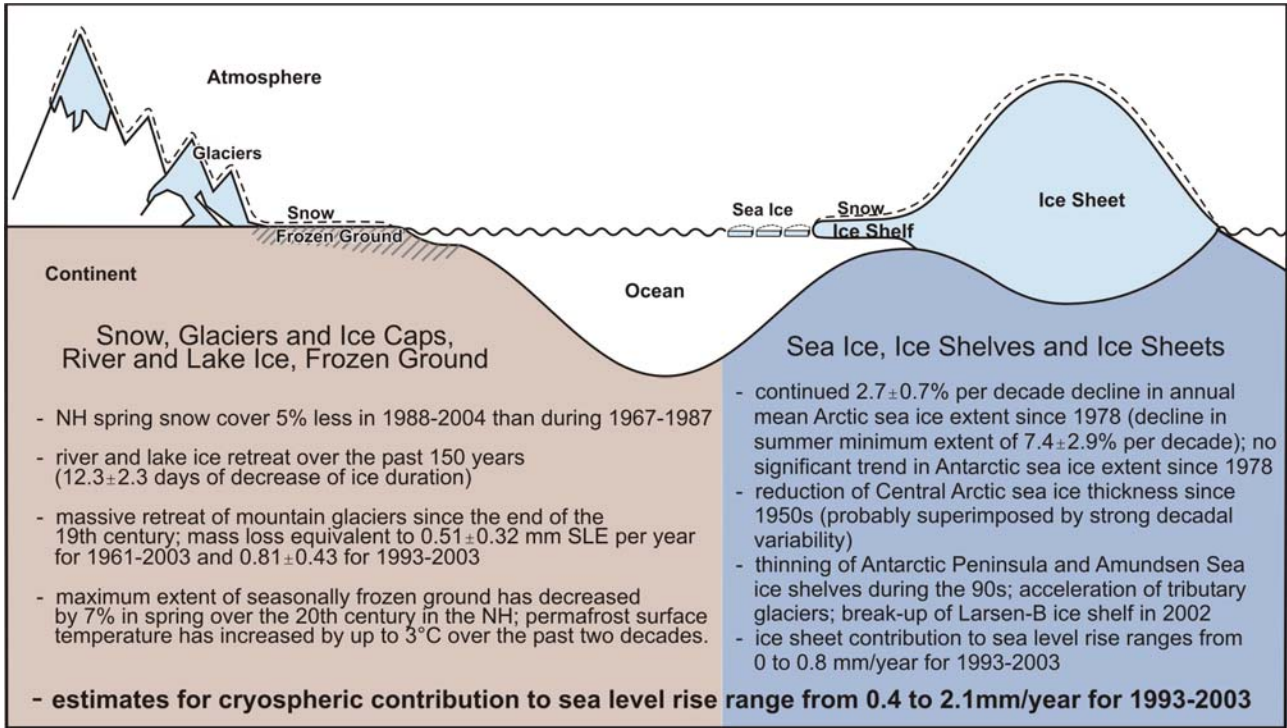
1
2



3
4
5
6
7
8
9

Figure 4.7.3. Historical variations of monthly area extent of seasonally frozen ground (including the active layer over permafrost) for the period from 1901 through 2002 in the Northern Hemisphere. The positive anomaly (blue) represents above monthly average area extent, while negative anomaly (red) stands for below average area extent. The time series is smoothed with a low-pass filter. (after Zhang et al., 2003).

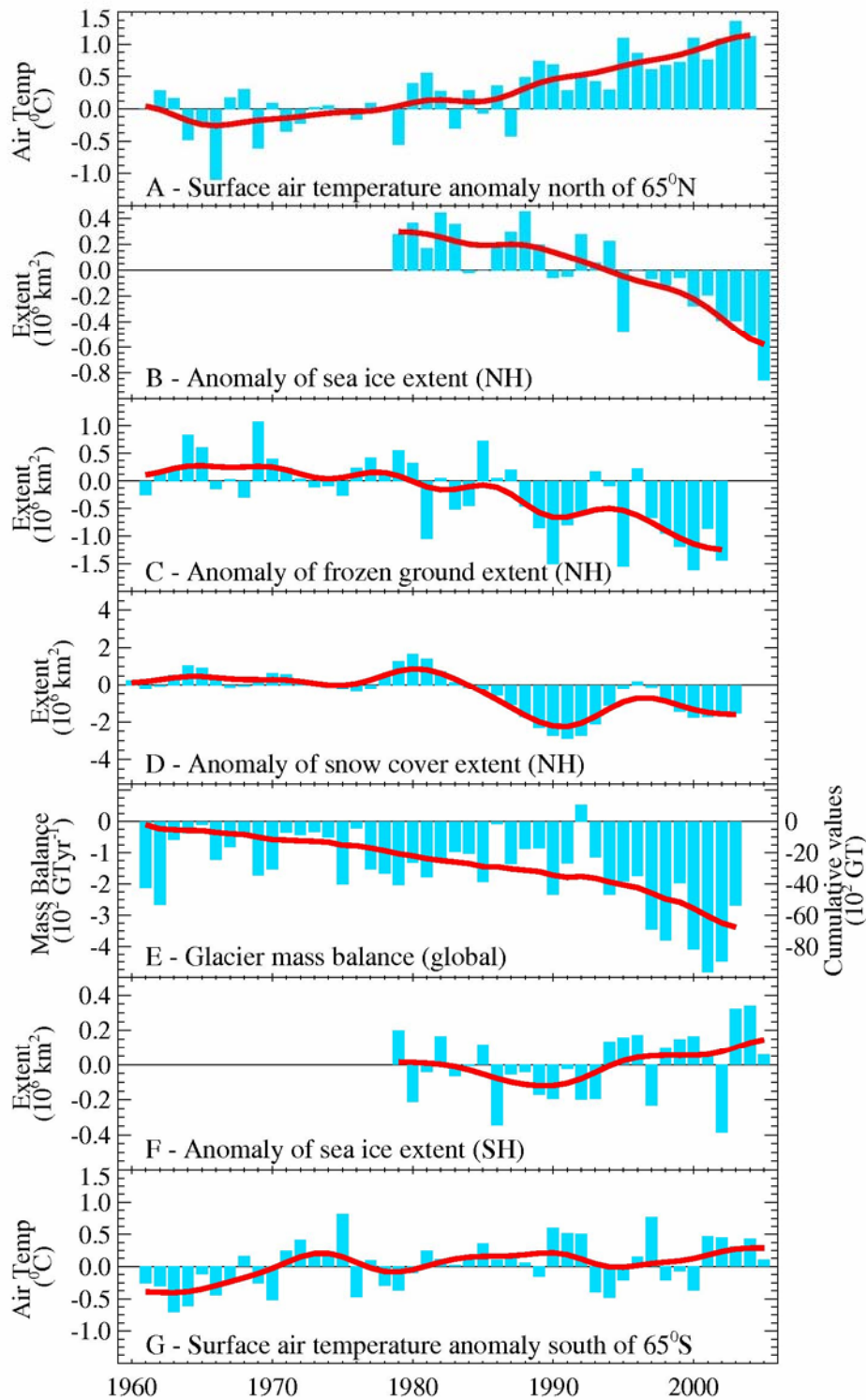
1
2



3
4
5
6

Figure 4.8.1. Summary of observed variations of the cryosphere.

1
2



3
4
5
6
7
8
9
10
11

Question 4.1, Figure 1. Anomaly time series of polar surface air temperature (A, G, updated from Jones and Moberg, 2003), Arctic and Antarctic sea ice extent (B, F, updated from Comiso, 2003), Northern Hemisphere (NH) frozen ground extent (C, Zhang et al., 2003), NH snow cover extent (D, updated from Brown et al., 2000) and global glacier mass balance (E, Ohmura, 2004; Cogley, 2005; Dyurgerov and Meier, 2005). The solid red line in E denotes the cumulative global glacier mass balance; otherwise it represents the smoothed time series using a 13-point filter (see Chapter 3).